AFRL-RI-RS-TR-2009-55
In-House Final Technical Report
March 2009

A SHORT-SEGMENT FOURIER TRANSFORM METHODOLOGY

APPROVED FOR PUBLIC RELEASE; DISTRIBUTION UNLIMITED.

STINFO COPY

AIR FORCE RESEARCH LABORATORY
INFORMATION DIRECTORATE
ROME RESEARCH SITE
ROME, NEW YORK

NOTICE AND SIGNATURE PAGE

Using Government drawings, specifications, or other data included in this document for any purpose other than Government procurement does not in any way obligate the U.S. Government. The fact that the Government formulated or supplied the drawings, specifications, or other data does not license the holder or any other person or corporation; or convey any rights or permission to manufacture, use, or sell any patented invention that may relate to them.

This report was cleared for public release by the 88th ABW, Wright-Patterson AFB Public Affairs Office and is available to the general public, including foreign nationals. Copies may be obtained from the Defense Technical Information Center (DTIC) (http://www.dtic.mil).

AFRL-RI-RS-TR-2009-55 HAS BEEN REVIEWED AND IS APPROVED FOR PUBLICATION IN ACCORDANCE WITH ASSIGNED DISTRIBUTION STATEMENT.

FOR THE DIRECTOR:

/s/

STEVEN JOHNS, Chief
Multi-Sensor Exploitation Branch

/s/

JOSEPH CAMERA, Chief
Information & Intelligence Exploitation Division
Information Directorate

This report is published in the interest of scientific and technical information exchange, and its publication does not constitute the Government's approval or disapproval of its ideas or findings.

REPORT DOCUMENTATION PAGE

Form Approved
OMB No. 0704-0188

1. REPORT DATE *(DD-MM-YYYY)*	2. REPORT TYPE	3. DATES COVERED *(From - To)*
MAR 2009	Final	Dec 06 – Dec 08

4. TITLE AND SUBTITLE

A SHORT-SEGMENT FOURIER TRANSFORM METHODOLOGY

5a. CONTRACT NUMBER
In House

5b. GRANT NUMBER
N/A

5c. PROGRAM ELEMENT NUMBER
62702F

6. AUTHOR(S)

Andrew J. Noga

5d. PROJECT NUMBER
459E

5e. TASK NUMBER
H7

5f. WORK UNIT NUMBER
C1

7. PERFORMING ORGANIZATION NAME(S) AND ADDRESS(ES)

AFRL/RIEC
525 Brooks Rd.
Rome NY 13441-4505

8. PERFORMING ORGANIZATION REPORT NUMBER
N/A

9. SPONSORING/MONITORING AGENCY NAME(S) AND ADDRESS(ES)

AFRL/RIEC
525 Brooks Rd.
Rome NY 13441-4505

10. SPONSOR/MONITOR'S ACRONYM(S)
N/A

11. SPONSORING/MONITORING AGENCY REPORT NUMBER
AFRL-RI-RS-TR-2009-55

12. DISTRIBUTION AVAILABILITY STATEMENT
APPROVED FOR PUBLIC RELEASE; DISTRIBUTION UNLIMITED. PA# 88ABW2009-0667

13. SUPPLEMENTARY NOTES

14. ABSTRACT

A short-segment Fourier-transform methodology is introduced. This method addresses the problem of reduced frequency resolution associated with desirable decreases in data segment lengths for accomplishing spectral analyses of sampled signals and data sequences. The method is characterized by user-defined sampling of the continuous-valued discrete-time Fourier transform, super-resolution in the frequency domain and allowance of Dirac delta functions associated with pure sinusoidal input data components.

15. SUBJECT TERMS

Signal processing, Discrete-time Fourier transform, Short-time Fourier transform, spectral estimation, spectrogram, Time-frequency representation, Matrix Pencil, Prony spectrum, Mated poles, Reduced bandwidth representation, Pencilgram, z-domain

16. SECURITY CLASSIFICATION OF:			17. LIMITATION OF ABSTRACT	18. NUMBER OF PAGES	19a. NAME OF RESPONSIBLE PERSON
a. REPORT	b. ABSTRACT	c. THIS PAGE			Andrew J. Noga
U	U	U	UU	41	19b. TELEPHONE NUMBER (*Include area code*) N/A

Table of Contents

List of Figures

1.0 Introduction

Considerable research effort has been expended in the general area of time-frequency signal analysis tools, and a wealth of published material exists as a result of these efforts. To date, this research can be characterized as a multiplicity of interrelated approaches to address the need for such tools. Most if not all of the approaches use some combination of three basic signal processing techniques: i) filtering, ii) demodulation, and iii) decomposition. The research reported herein falls into the latter category of signal decomposition.

Included among the approaches that became widely used by practitioners is the band-pass filtering and envelope demodulation approach. This approach became particularly popular in hardware instruments provided by test equipment manufacturers, due to its simplicity and effectiveness. The more popular example is that of the spectrum analyzer used by communications engineers. These devices essentially consist of a fixed frequency narrow-band band-pass filter that precedes an envelope/amplitude demodulator. The input signal is translated in frequency using nonlinear mixing with a swept local oscillator prior to band-pass filtering. Rapidly repeated sweeps thereby allow for an "instantaneous" determination of the frequency content across the frequency band of interest.

From a research perspective, a sub-category of approaches has become very popular and can be characterized by their use of instantaneous frequency concepts. (For a single carrier component modulated in either phase or frequency, measurement of the instantaneous frequency constitutes FM demodulation [Noga].) These approaches are generalized in the sense that for signals modeled as consisting of multiple modulated carrier components existing simultaneously, the goal is to demodulate each of these components. The instantaneous frequency of each component is of particular interest as a time-frequency (or more correctly, time-instantaneous frequency) representation of the input signal. This is an important distinction to make regarding the various signal analysis tools that exist. Researchers that employ techniques from this instantaneous-frequency-based sub-category are often interested in using the resulting time-frequency representation to determine how the signal was created. For example, analyzing a music signal consisting of the recording of a flute may allow for automatically determining the sequence of notes that were played to create the music. In this form of signal analysis, the true spectral content is not necessarily of interest. As another example, consider similar analysis of a frequency-shift-keyed (FSK) communication signal. For communication purposes, determining the shift frequencies as a function of time is analogous to determining the notes as a function of time in the previous music signal example. However, communication designers have to work under various constraints, including constraints on bandwidth and spuriously generated signals.

Therefore, although demodulation is of interest at the intended receiver of the FSK signal, spectral content outside the location of the instantaneous frequencies is also of interest to prevent interference to other users in adjacent channels. For the music signal, an example of where the true spectral content is of interest would be in analyzing tonal quality of the flute. It can be expected that variations in tonal quality would be reflected not only in the instantaneous frequencies, but also in the spectral regions outside these frequencies.

Popular approaches to signal decomposition can also lead to time-frequency representations. Example methods of signal decomposition include wavelet decomposition, and sinusoidal basis function decomposition as when using the discrete Fourier transform (DFT) or the fast Fourier transform (FFT). Of particular interest in this report is the FFT-based method referred to as the spectrogram. Due to its computational simplicity and relative output quality, the spectrogram has become a highly favored tool for spectral analyses. The spectrogram of a signal is calculated starting with the selection of a signal segment length, L. The sequential values resulting from uniform sampling of the signal (i.e., the sampled signal) are separated into consecutively indexed segments. Each segment contains a subset of sequential samples from the original sequence. The subsets are chosen to start at sample indices that increase as the segment index increases, and are often overlapping. (In this report, a 50% overlap is used and segment indices start at one and increase by 0.5 for axis labeling purposes.) With the selection of segment length and the separation into segments, an FFT is calculated for each segment. The resulting magnitude values for each frequency bin from consecutive segments are plotted versus segment index to form the spectrogram.

The published results in the above areas are both numerous and high in quality. General reference is made to [Cohen], [Oppenheim] and [Suter] for background in some of the various existing approaches. More directly related background for the research in this report can be found in [Kay].

1.1 A Short Segment Fourier Transform

For direct comparison to the spectrogram, the same segmentation process previously described is used to generate the new time-frequency representation developed in this research. Because the new technique also represents an estimation of the true Fourier transform of each segment, it is by definition continuous in the frequency variable. To further allow for direct comparisons and for practical purposes, the estimated Fourier transform of each segment is sampled in frequency at uniform spacing over the $[0, 2\pi)$ frequency interval.

The intent of the new approach is to overcome a characteristic problem associated with the FFT-based spectrogram. Specifically, as segment lengths decrease for more time resolution, frequency resolution degrades in the spectrogram. An approach similar to that taken here is presented in [Kay]. Important differences will be summarized in the concluding section of this report.

2.0 Reduced Bandwidth Representation

To develop a reduced bandwidth (Fourier) representation of any given signal segment, we first consider the response, $z/(z-a)$, for an example pole, $a = \exp(j\pi/4)$. Shown in Figure P-1 is the magnitude of this response for a limited amplitude range of 110 dB. The amplitude range is intentionally limited to emphasize the shape of the response both near the pole and near $z = 0$. It is also useful to limit the amplitude range given that the magnitude response at the pole is infinite in value. Referring to the figure, we note that the response in the vicinity of the pole is very distinct and non-zero. The response evaluated on the unit circle at $z = \exp(j\omega)$ is the (discrete-time) Fourier transform, and is of particular interest. Our given pole response is that of a unilateral complex sinusoid, thus the peak on the unit circle at the pole is due to the sinusoidal nature of the signal sequence. The response on the unit circle near the peak is partly due to the sharp transition of the sequence as the sinusoid starts. Various definitions of signal bandwidth exist to help identify the frequency region of significant spectral content about the center frequency at the pole peak. We will be able to leverage these observations and definitions to define a corresponding response of reduced bandwidth after first considering the individual real and imaginary responses of our example. Shown in Figure P-2 is the magnitude of the imaginary part of the example response, $z/(z-a)$. Once again, the amplitude range is arbitrarily chosen for plotting purposes. It is immediately apparent that the imaginary part of the response contributes to the Fourier transform in the vicinity of the peak, and therefore to the signal bandwidth. This motivates us to further consider the magnitude of the real part of the response as presented in Figure P-3. This figure is particularly revealing in that the unit circle is seen to have an apparent constant low-level response, with the exception of the sharp peak at the pole. Observations of the actual numerical values of this response on the unit circle reveals that the peak occurs in a very tight frequency region. Small (machine epsilon) deviations from the pole frequency change the response from infinity (not-a-number or NaN) at the pole, to a magnitude of 0.5 elsewhere. Motivated by this and previous observations regarding the imaginary part of the response, we consider defining a *reduced bandwidth representation* frequency response as

$$S_a\left(e^{j\omega}\right) = Re\{z/(z-a)\}|_{z=e^{j\omega}} - 0.5 \ . \tag{2-1}$$

The magnitude of such a response is shown in Figure P-4. Note that the magnitude response on the unit circle is distinctly apparent and small in value, and is confirmed to be zero at all frequencies except the exact value (within machine epsilon deviations) of the pole frequency. It is also interesting to note that similar functions have been sought for related but distinct purposes, in defining non-zero regions for time-frequency distributions. The visual appearance of these similar functions have led authors to refer to them as “bowtie” functions for obvious reasons. (See e.g., [Boashash], [Brown]). As a distinction, the “bowtie” response shown in the figure is noted to have an infinite peak at the pole (as opposed to some finite value sometimes cited in the references).

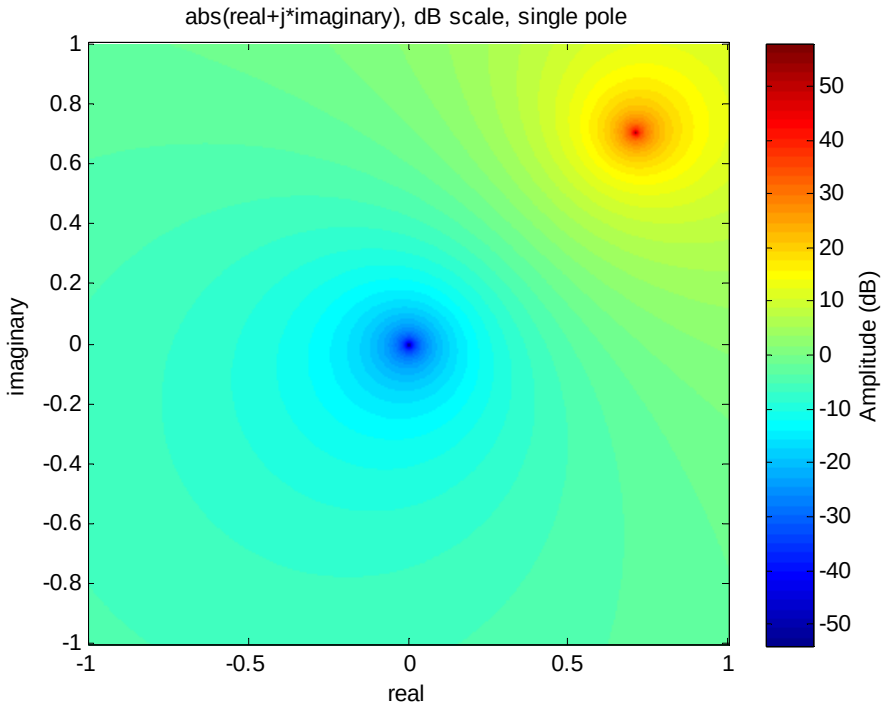

Figure P-1. Magnitude plot of a single pole at $\omega = \pi/4$ on the unit circle of the z-plane.

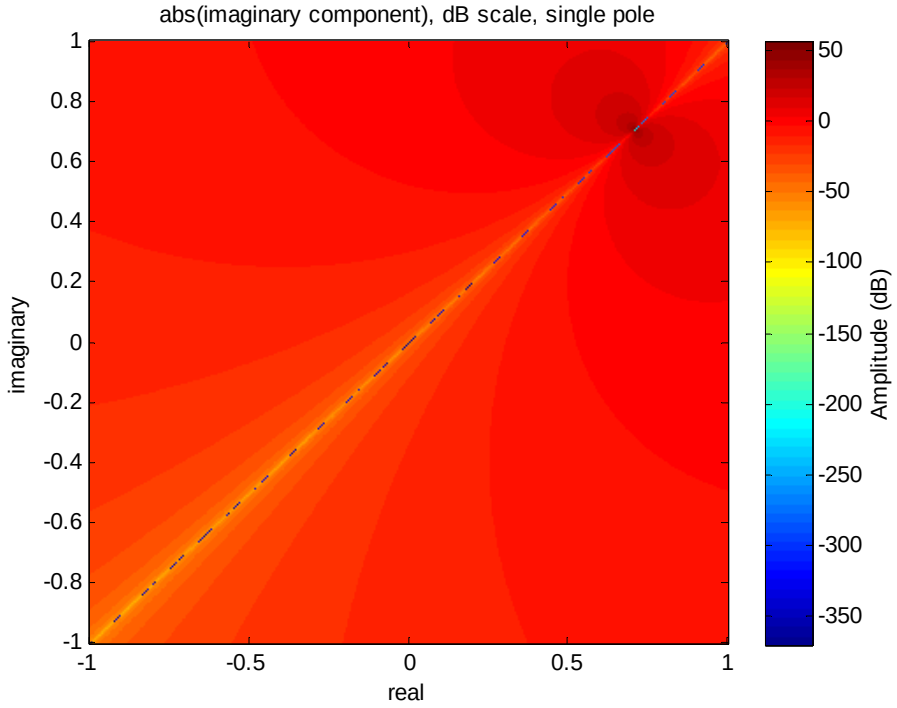

Figure P-2. Magnitude plot of the imaginary component of a single pole at $\omega = \pi/4$ on the unit circle of the z-plane.

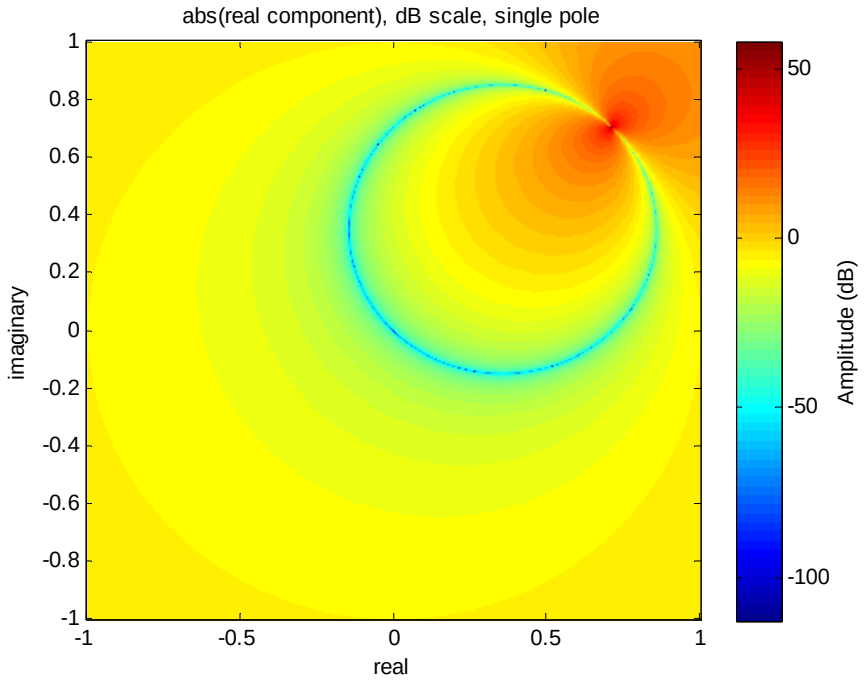

Figure P-3. Magnitude plot of the real component of a single pole at $\omega = \pi/4$ on the unit circle of the z-plane.

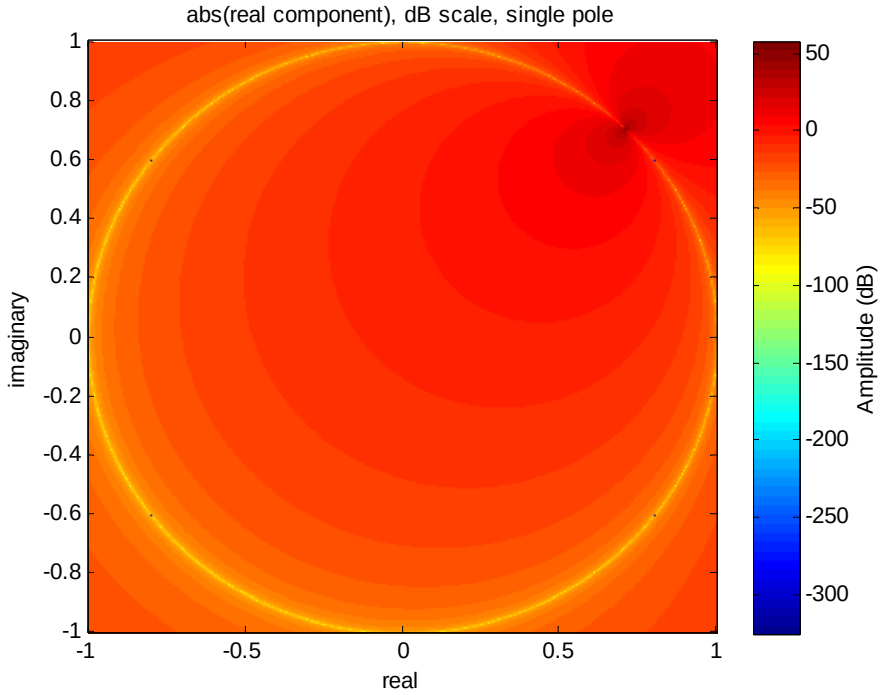

Figure P-4. Magnitude plot of the real component of a single pole at $\omega = \pi/4$ on the unit circle of the z-plane, with .5 bias removed.

2.1 Mated Poles

Having defined the reduced bandwidth representation for a single pole as in Eq. (2-1), we need to identify the mathematical/physical interpretation of such a representation. We begin by defining

$$Y_a\left(e^{j\omega}\right) = \frac{1}{2}Y_1\left(e^{j\omega}\right) + \frac{1}{2}Y_2(e^{j\omega}) \ , \tag{2-2}$$

where

$$Y_1\left(e^{j\omega}\right) = \left[\frac{z}{z-a}\right]\Big|_{z=e^{j\omega}} \tag{2-3}$$

and

$$Y_2\left(e^{j\omega}\right) = Y_1^*(e^{j\omega}) \tag{2-4}$$

is the conjugate of Y_1. From Eqs. (2-3) and (2-4), Eq. (2-2) is equivalent to the first term of Eq. (2-1). Substituting from Eqs. (2-3) and (2-4) into Eq. (2-2) and simplifying results in

$$Y_a(z)|_{z=e^{j\omega}} = 0.5\left[\frac{z}{z-a} + 1 + \frac{-z}{z-\frac{1}{a^*}}\right]\Bigg|_{z=e^{j\omega}} . \tag{2-5}$$

Replacing the first term of Eq. (2-1) with the results from Eq. (2-5) we obtain

$$S_a\left(e^{j\omega}\right) = 0.5\left[\frac{z}{z-a} + 1 + \frac{-z}{z-\frac{1}{a^*}}\right]\Bigg|_{z=e^{j\omega}} - 0.5 \ . \tag{2-6}$$

From Eq. (2-6) we see that the reduced bandwidth representation of a single pole can be interpreted as the response of a two pole system. The poles of this new system are identified as the original pole, a, and the conjugate of its reciprocal, $1/a^*$. Herein, these poles will be referred to as *mated poles*.

Shown in Figure P-5 is the imaginary component of the mated pole response $Y_a(z)$, for a specific example, $a = e^{\alpha+j\omega}$, with $\alpha = .1$ and $\omega = \pi/4$. Note that the mated poles occur at the same frequency, but at radial distances from the origin that are reciprocal in magnitude. This is easily confirmed by the fact that $\frac{1}{a^*} = e^{-\alpha+j\omega}$. Figure P-6 presents the magnitude of the Fourier transform of a single pole, and that of the associated reduced bandwidth representation. The blue-colored response represents the original single pole frequency response, and the red-colored response represents that of the reduced bandwidth response. For this example, $\alpha = -0.3$ and $\omega = \pi/4$, with 1024 uniformly spaced samples selected on the unit circle. As seen in the figure, the mated pole response with bias removal is significantly reduced in bandwidth.

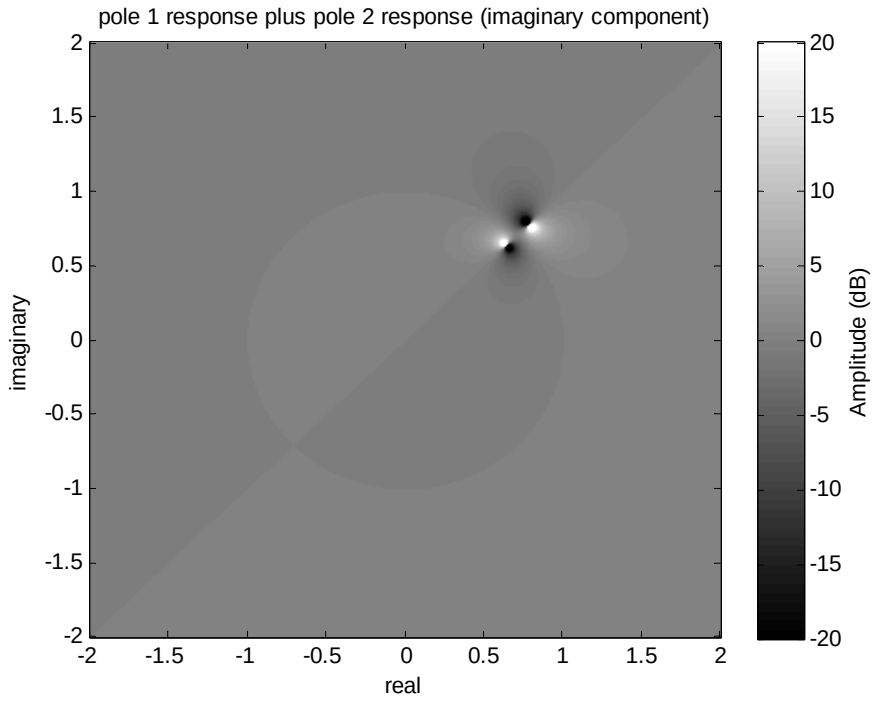

Figure P-5. Imaginary component of z-plane response of mated poles for $\alpha = .1$ and $\omega = \pi/4$ radians.

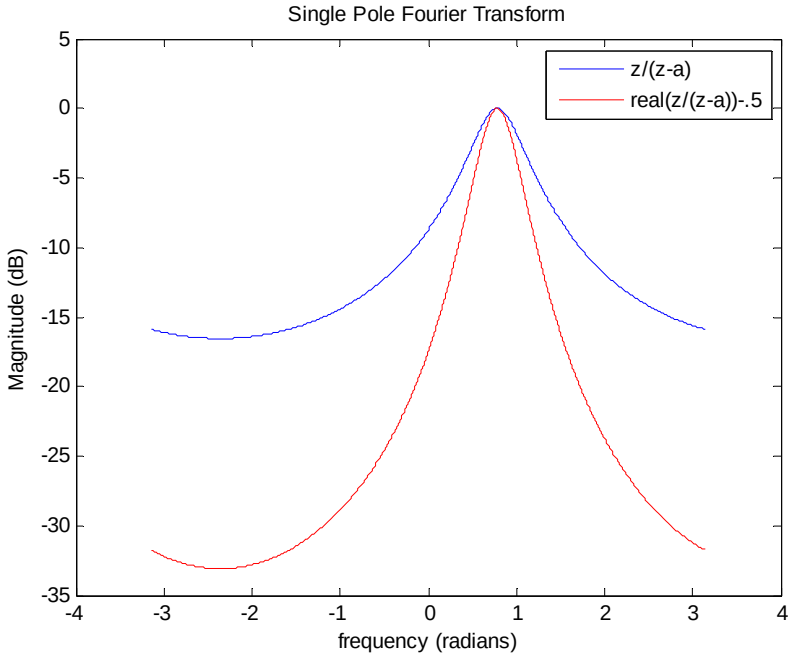

Figure P-6. Fourier transform and Reduced Bandwidth Representation Fourier transform for a single pole at $\omega = \pi/4$ and $\alpha = -0.3$, sampled at N = 1024 points on the unit circle.

Another specific example is presented in Figure P-7. In this case, $\alpha = 1e^{-3}$ and $\omega = \pi/4$, with 1024 uniformly spaced samples selected on the unit circle. Note that as the original pole approaches the unit circle both responses sharpen as expected, however, the reduction in bandwidth becomes more pronounced. To gain further insights, we are interested in the inverse z-transform of our mated pole response identified by Eq. (2-5).

Consider the case where $a = e^{\alpha + j\omega}$ is inside the unit circle, i.e., $\alpha < 0$. The region of convergence (ROC) associated with the term $z/(z-a)$ for this case is $|z| > |a|$. The ROC for this term extends from (but not including) a ring of radius equal to the pole magnitude, outwards in all directions on the z-plane, and includes the unit circle. The inverse z-transform for this term of the response is well known, and is equal to $a^n u[n]$. The ROC associated with the term $-z/(z - 1/a^*)$ for this case is $|z| < |1/a^*|$. It extends from (but not including) a ring of radius equal to the magnitude of the pole $1/a^*$, inwards on the z-plane towards zero, and also includes the unit circle. The inverse z-transform for this term of the response is also well known, and is equal to $a^n u[-n-1]$. The remaining term is a constant with a ROC that includes the entire z-plane, and is known to have a Kronecker delta function, $\delta[n]$, as its inverse. Combining terms, the superposition principle allows us to write

$$y[n] = 0.5(a^n u[n] + \delta[n] + (1/a^*)^n u[-n-1]) \; . \tag{2-7}$$

Thus our mated poles result in the sum of a right-sided sequence due to the pole inside the unit circle, a Kronecker delta sequence, and a left-sided sequence due to the pole outside the unit circle. From Eq. (2-7) and the relationship between $Y(e^{j\omega})$ and $S(e^{j\omega})$ given in Eqs. (2-5) and (2-6) allows us to write

$$s[n] = 0.5(a^n u[n] + (1/a^*)^n u[-n-1]) \; . \tag{2-8}$$

This is our sequence resulting from the reduced bandwidth representation of the original signal. Such a sequence is shown in Figure P-8, with the scale factor of ½ omitted. The interpretation of the result in the sequence domain is that the reduced bandwidth representation leads to a corresponding sequence that exists for all indices, n. For the example shown in the figure, the red- and magenta-colored dots are respectively the real and imaginary parts of the right-sided component, and the blue- and cyan-colored dots are respectively the real and imaginary parts of the left-sided component. In this example, $\alpha = -.05$ and $\omega = \pi/34$. The case where the pole, a, is outside the unit circle (i.e. the original sequence is left-sided) can be analyzed in a similar fashion, but the basic results are the same.

In the sequence domain, the signal sequence no longer has an abrupt start near index 0, thereby reducing potentially extraneous bandwidth in the Fourier domain. Also, the new sequence is seen to be symmetric in magnitude.

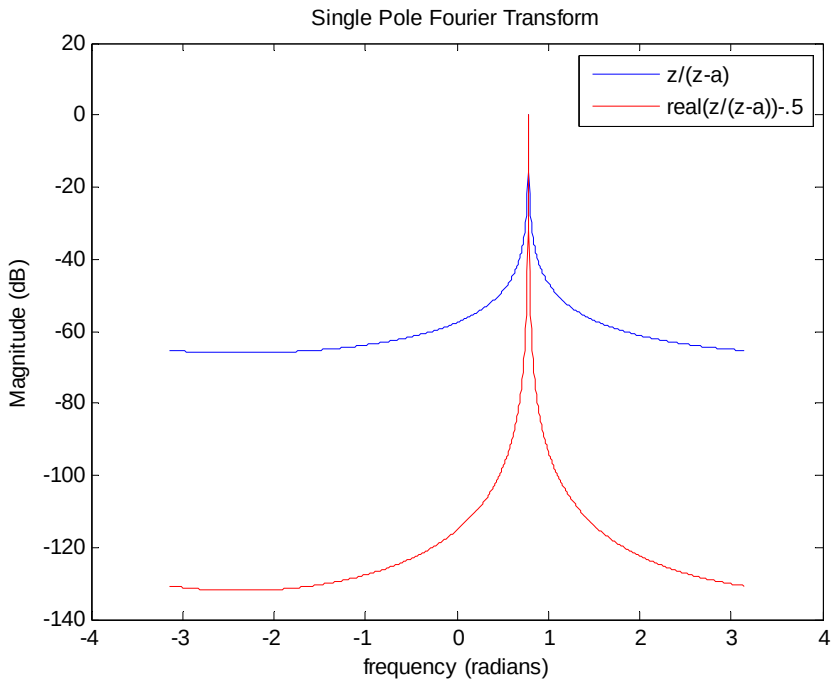

Figure P-7. Fourier transform and reduced bandwidth representation Fourier transform for a single pole at $\omega = \pi/4$ and $\alpha = 1e^{-3}$, sampled at N = 1024 points on the unit circle.

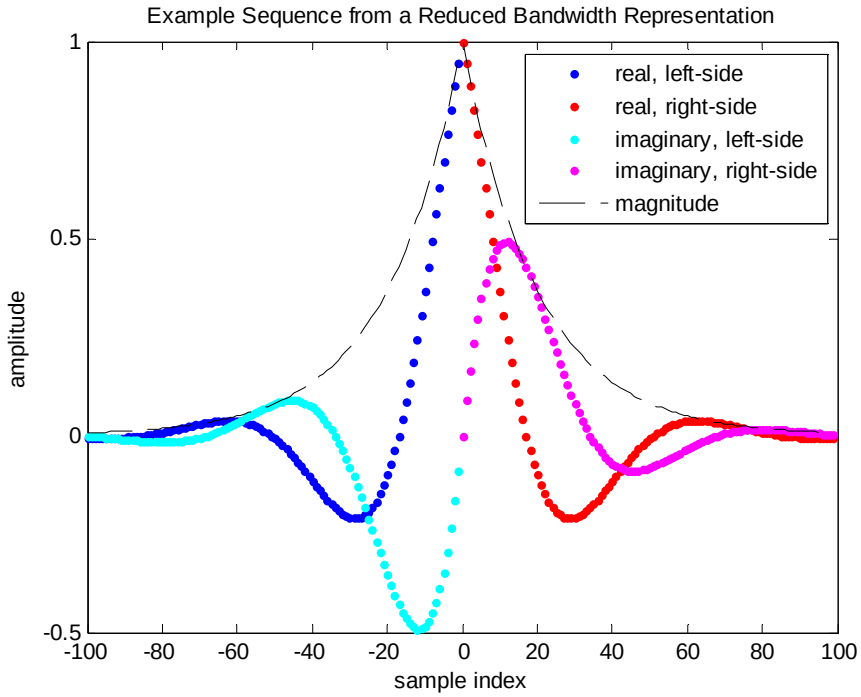

Figure P-8. An example sequence resulting from a reduced bandwidth representation for a decaying (right-sided sequence) with $\alpha = -.05$ at a frequency of $\omega = \pi/34$ radians.

3.0 Application and Results

Before presenting results from various test signal inputs, a generalization of the reduced bandwidth representation is required. The Fourier-transform of our input sequence segment, $x[n]$, can be decomposed as

$$X(e^{j\omega}) = X_d(e^{j\omega}) + X_g(e^{j\omega}) \,, \tag{3-1}$$

where

$$X_d(e^{j\omega}) = \sum_i A_i X_i(e^{j\omega}) \tag{3-2}$$

is the sum of the Fourier-transforms of each right-sided component, $x_i[n] = {a_i}^n u[n]$, and

$$X_g(e^{j\omega}) = \sum_k A_k X_k(e^{j\omega}) \tag{3-3}$$

is the sum of the Fourier-transforms of each left-sided component, $x_k[n] = {a_k}^n u[-n-1]$. The (complex valued) factors, A_i and A_k, are the amplitudes of the right-sided and left-sided components respectively. From Eq. (2-5) along with Eqs. (3-1) through (3-3), it can be shown that the Fourier transform resulting from the combined mated pole responses is

$$Y(e^{j\omega}) = \sum_i A_i\left(Re\{X_i(e^{j\omega})\}\right) - \sum_k A_k\left(Re\{X_k(e^{j\omega})\}\right) \,. \tag{3-4}$$

Finally, corresponding to Eq. (2-1) we obtain the reduced bandwidth Fourier representation

$$S(e^{j\omega}) = \sum_i A_i(Re\{z/(z-a_i)\}|_{z=e^{j\omega}} - 0.5) - \sum_k A_k(Re\{z/(z-a_k)\}|_{z=e^{j\omega}} - 0.5) \,. \tag{3-5}$$

It should be noted that in deriving Eq. (3-5), we have ignored any sequence shift associated with each of the left-sided components that arises due to the length of the segment, *L*, being analyzed. Unless otherwise specified, application results presented herein ignore the effects of this shift. For some uses of the reduced bandwidth Fourier representation, taking this shift into account may be appropriate. This may be particularly true when considering implementations of filtering in the Fourier domain via products of transforms. Determining the potential for such use is reserved for future research. For this report, the factor required to account for this shift is omitted to avoid ripple artifacts in magnitude spectra that can be visually distracting.

3.1 Signal Segment Decomposition

To make use of the above results, a method of decomposing an input signal data segment into component right- and left-sided exponential sequences is required. Relevant methods do exist and are found in the literature. However, the methods typically decompose into decaying right-sided exponentials only, or decompose into decaying and/or growing right-sided exponentials. One such method is the Matrix Pencil (MP) algorithm (See e.g. [Sarkar]), and is

adopted for use in this research. The MP algorithm is attractive in that it directly yields most of what is required to estimate the reduced bandwidth Fourier representation. In particular, the MP algorithm will generate estimates of the parameters $\{|A_i|, \varphi_i, \alpha_i, \omega_i\}$ for the decaying and/or growing right-sided complex exponentials. These parameters are the component magnitude, phase (in radians), decay (or growth) and radian frequency respectively. Note that the complex valued amplitude can be also represented as $A_i = |A_i|e^{j\varphi_i}$. For the growing right-sided complex exponentials, i.e., the components where $\alpha_i > 0$, the conversion required is

$$A_k = (A_i/a_i)e^{a_i L} = A_i e^{a_i(L-1)} \,. \tag{3-6}$$

Eq. (3-6) is applied to the amplitude parameters generated by the MP algorithm, for the growing components. The remaining parameters are unchanged, and are associated with the corresponding converted component as indexed by the variable k.

The MP algorithm allows for user-selection of the total number of components, K_c, and allows for up to $L/2$ components to be specified. For our purposes, a variant of the MP algorithm has been created that allows for user specification of up to $\left(\frac{L}{2}\right) - 1$ components, to help mitigate instabilities that can otherwise occur. These instabilities are detected and then avoided by increasing the specified number of components by 1, as used in [Haddad].

Thus we can use the Matrix Pencil algorithm for signal segment decomposition and use the associated parameter estimates to generate a reduced bandwidth Fourier representation for consecutive signal segments. The resulting time-frequency representation is referred to herein as the *pencilgram*.

3.1.1 Decomposition Iterations

To mitigate concerns regarding the accuracy of signal models and decompositions employed in this research, a simple iteration technique has been developed. Unless otherwise specified, this iteration technique is applied to the multi-segment examples presented herein. In particular, a two-pass iteration is used to address model inaccuracies as a result of limitations on the number of signal components, K_c.

3.2 Example Pencilgrams

While specific metrics could be introduced to assess the performance of any given time-frequency representation, such metrics tend to be relevant only to a subset of signal scenarios. For example, one could consider single-tone input tests for assessing frequency resolution and second-order harmonic distortion. Likewise, two-tone tests could be devised to assess third-order distortions. Such objective tests of the pencilgram and other reduced bandwidth Fourier representations are reserved for future research. In lieu of specific metrics, the signal processing community has often relied on subjective analyses of signals of interest when evaluating time-frequency representations. To demonstrate the potential benefits of the pencilgram, the latter approach is taken for this report.

3.2.1 Kay and Marple Test Signal Segment

First, we can leverage published subjective comparisons as applied to a specially constructed test signal proposed in [Kay]. This signal consists of a band-limited (band-pass) noise process centered at 0.7π radians plus three tones, each at 0.2π, 0.4π and 0.42π radians. The amplitudes of the sinusoids were 0.1, 1.0 and 1.0 giving rise to +10, +30 and +30 dB signal-to-noise power ratios respectively. The segment length is $L = 64$. (No other information was given regarding the filter used to generate the band-pass noise.) Shown in Figure KM-1 is the Fast Fourier-Transform- (FFT-) based spectral estimate of the test signal. The samples were not weighted prior to the FFT (i.e., a rectangular window was used), nor was zero-padding employed. Because of the short segment length, frequency resolution is limited as seen in the figure. In particular, although the first tone is distinguishable as a component, the two remaining tones are too close in proximity to be able to distinguish them as separate signal components. The energy due to the band-pass noise is also apparent, although it would be difficult from this figure to identify this component as band-pass noise; it could erroneously be identified as an additional four or five sinusoids. This may be related to the order and type of filter used to filter the noise. For example, a high order (relative to *L*) finite impulse response (FIR) filter would require a longer segment to allow the FFT to give a more accurate representation of the filter shape. This fact combined with the nature of the noise signal itself, would not lead one to expect to see the filter shape alone as implied in the reference, but rather the product of the filter response and the true underlying noise spectrum for a given segment length. Thus at best, we would only expect to see something similar to what is observable in the figure for the band-pass noise. Note in particular that the FFT-based spectral estimate does fairly well with regard to the strengths of the sinusoids; they are commensurate with the known signal strengths.

For comparison, the (single segment) pencilgram of the same sequence is shown in Figure KM-2. For this pencilgram, 18 poles are requested and the frequency response is generated via 5000 uniformly spaced samples on the unit circle. Sharp peaks are noted at the locations of the true sinusoids, and the shape of the band-pass noise is apparent. Note that the magnitude range on this figure is 50 dB greater than that of the previous figure. Overall, the pencilgram for this sequence compares favorably with the FFT-based method, however, it is noted that the magnitudes of the sinusoidal components are much larger than that of the FFT-based method. It is also interesting to note that increasing the number of requested poles to 31 further sharpened the response due to the sinusoids, and also increased their associated magnitudes. In general, as poles approach the unit circle, they give rise to large amplitudes in very small frequency ranges.

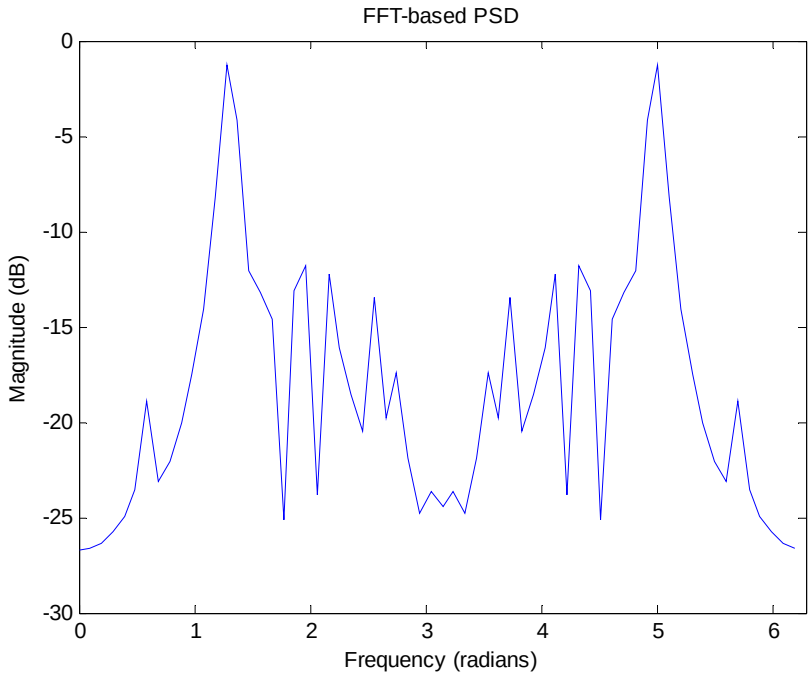

Figure KM-1. An FFT-based spectral estimate of the test signal identified in [Kay]; rectangular data window used and no zero padding.

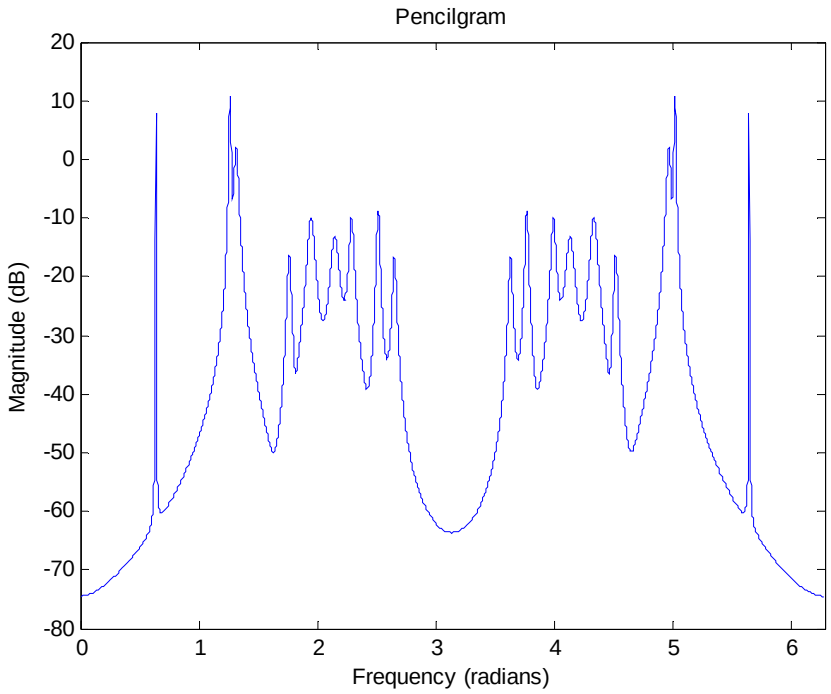

Figure KM-2. Pencilgram of the test signal identified in [Kay]; Kc = 18 complex exponential components requested with 5000 samples on the unit circle.

3.2.2 Sinusoid and Growing Right-Sided Exponential Signal Segment

The next example consists of a unit amplitude sinusoid at $.2\pi$ radians plus a single complex exponential component. The complex exponential has an amplitude of 1 (prior to amplitude conversion), with $\alpha = .09$ at a frequency of $\omega = 1.4$ radians. Note that the left-sided representation of this signal has a frequency of -1.4 radians, which will peak at $2\pi - 1.4$ radians, due to the modulo nature of the frequency response. The FFT-based spectral estimate is presented in Figure KM-3. From this figure it is apparent that because of the overwhelming strength of the exponential component relative to the sinusoid, the sinusoid itself is barely detectable as a small glitch in the spectrum at the expected locations of $.2\pi$ and $2\pi - .2\pi = 1.8\pi$ radians.

The (single segment) pencilgram of this same sequence is presented in Figure KM-4. Both components are clearly distinguishable. We once again note that the pole estimate that is near the unit circle due to the sinusoidal component, leads to large amplitude peaks approximating Dirac delta functions. Thus, the function identified in Eq. (2-1) can be considered a nascent (Dirac) delta function. More will be discussed later in this report regarding this property.

3.2.3 Multi-Segment Sinusoid

We now progress to test signals that are more substantial in length, and analyzed by partitioning the sequence into consecutive overlapping segments of short length. The overlap for all subsequent examples is 50%, and segment lengths are $L = 64$ samples. It should also be noted that these pencilgrams have been generated as a result of a 2-pass Matrix Pencil method described previously. The number of uniformly spaced samples on the unit circle, *N*, is specified as 1024 for the pencilgrams. All spectrograms presented for comparisons were calculated using Hanning window weighting and were zero-padded to length *N*=1024.

The first such example is a pure sinusoid at $\omega = 66\pi/N$ radians, and is shown in Figure S-1. The upper subplot is the pencilgram and the lower subplot is the FFT-based spectrogram. For comparison purposes, the amplitude (magnitude) range on both subplots was set from -40 to +40 dB. Careful inspection of the pencilgram shows a sharp line at the correct frequency. All signal energy is contained at this frequency index, and all others contain no measurable energy. In contrast, the spectrogram has substantial energy spread in FFT frequency bins at and around the correct frequency. Also, the spectrogram contains signal energy in all other frequency bins resulting from assumed segment periodicity and the implicit convolution of the frequency response of the window with that of the data. Figure S-2 shows the spectrogram of the original signal and the spectrogram of the error associated with the MP signal model. As seen in figure, the signal model for this example is highly accurate.

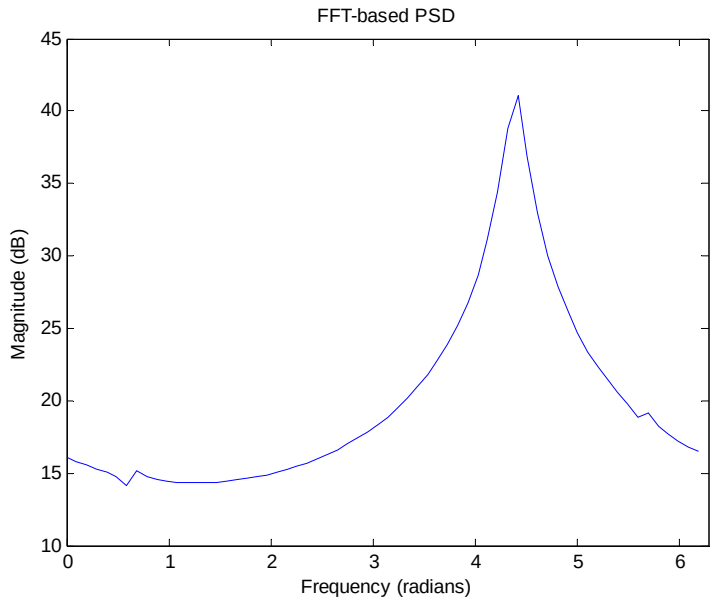

Figure KM-3. An FFT-based spectral estimate of a test signal consisting of a unit amplitude sinusoid at $\omega = .2\pi$ radians plus a unit amplitude growing (right-sided) complex exponential with $\alpha = .09$ and frequency of 1.4 radians; rectangular data window used and no zero padding.

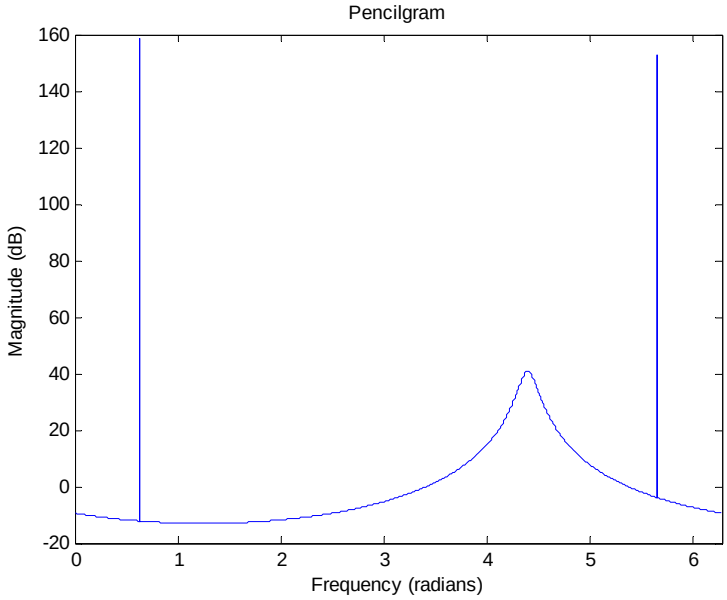

Figure KM-4. Pencilgram of a test signal consisting of a unit amplitude sinusoid at $\omega = .2\pi$ radians plus a unit amplitude growing (right-sided) complex exponential with $\alpha = .09$ and frequency of 1.4 radians; Kc = 18 complex exponential components requested with N = 5000 samples on the unit circle.

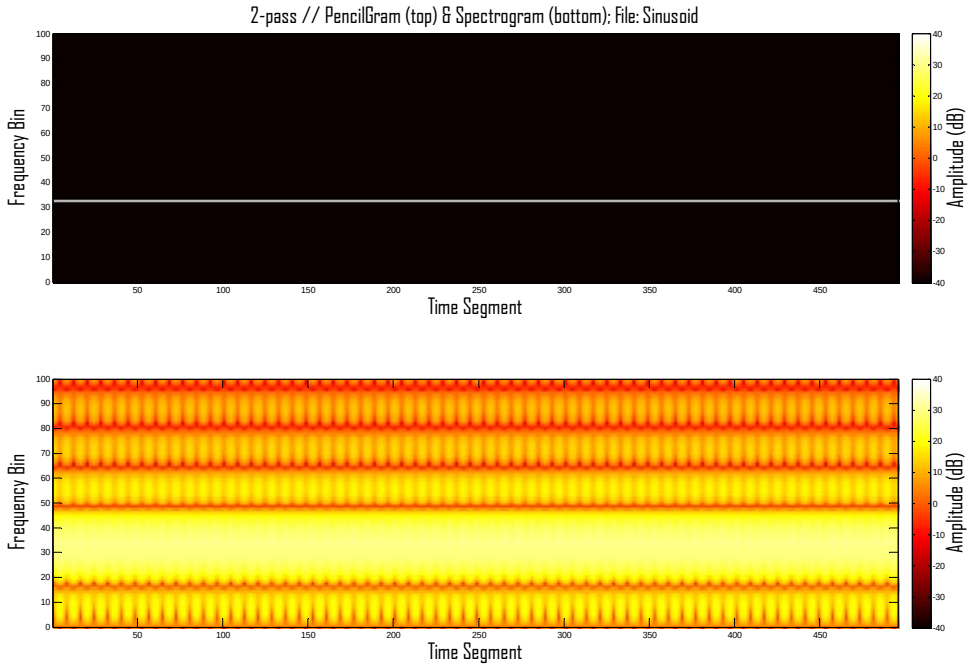

Figure S-1. Pencilgram (upper subplot) and Spectrogram (lower subplot) of a sinusoidal input test signal; 2x28=56 complex exponential components requested for the pencilgram; frequency bins 0 to 100 shown and color-map chosen for visibility.

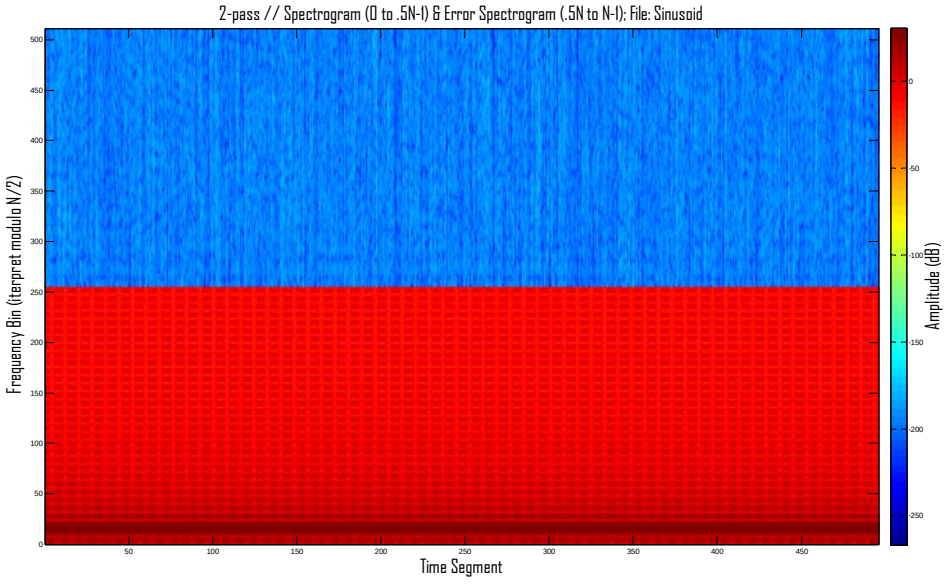

Figure S-2. Spectrogram of error signal (bins .5N to N-1) and spectrogram of sinusoidal input test signal (bins 0 to .5N-1); 2x28=56 complex exponential components requested for the pencilgram.

3.2.4 Multi-Segment Chirp

For this example, a chirp signal (a single swept frequency) is used to generate both the pencilgram and FFT-based spectrogram as shown in the corresponding subplots of Figure C-1. Once again, the amplitude (magnitude) range is set from -40 to 40 dB for comparisons. The modulation index is intentionally chosen to be large to concentrate energy near the instantaneous frequency. Referring to the spectrogram, while we expect some energy spread near the peak energy, again the implicit segment periodicity and data window convolution produces significant spectral artifacts throughout the spectrum. In contrast, the pencilgram shows significant energy near the peak and quickly subsides outside this location. This is true for all time segments. Looking across time segments, a variation is noted in this spread of energy away from the peak. However, it is also pointed out that the level of this energy (shown in bright blue) is about 30 dB lower than that of the spectrogram. This is an example where a more detailed analysis could be performed to obtain objective metrics regarding this apparent spectral spread. In particular, the true spectrum determined analytically could be compared to the results obtained in the pencilgram. Such objective analyses, now motivated by the subjective results, are reserved for future research. Shown in Figure C-2 is the spectrogram of both the error due to MP modeling inaccuracy and the original signal. Again note that the MP model is quite accurate as indicated by the level of the error signal relative to the original. This is accomplished in this example with 14 components requested per iteration, leading to potentially 2(1+14) = 30 complex sinusoids generated by the MP algorithm. Note that up to 32 components could have been generated by the MP algorithm for each 64 sample segment per iteration. Thus for two iterations as used in this example, 64 complex sinusoids and associated parameters could have been generated.

As previously described, the phase factor $e^{-j\omega L}$ has been omitted in our development of the reduced bandwidth representation. Comparing the results shown in Figures C-3 and C-4, we observe that incorporation of this factor changes the corresponding pencilgram. Figure C-3 shows the pencilgram without this factor, and Figure C-4 shows the pencilgram incorporating this factor for all left-sided components in the decomposition. The merit in incorporating this phase factor is left for further study; this analysis is expected to benefit from the development of the objective metrics already alluded to.

Results from a variation of the chirp test signal are also presented here. This variation is a band-pass filtered version of the previously described chirp signal. The band-pass filter used to generate this signal is an Butterworth infinite impulse response (IIR) filter as given by the Matlab command `[bfilt,afilt]=butter(16,[.4 .6])`. This command generates a 16^{th} order band-pass filter centered at the middle of the Nyquist band, with 200 dB attenuation at $.2\pi$ and $.8\pi$ radians, and over 400 dB attenuation at the band edges. Figures FC-1 and FC-2 show the results. Note that the pencilgram gives intuitively satisfying results, whereas the spectrogram again has significant artifacts that obfuscate the true spectral content.

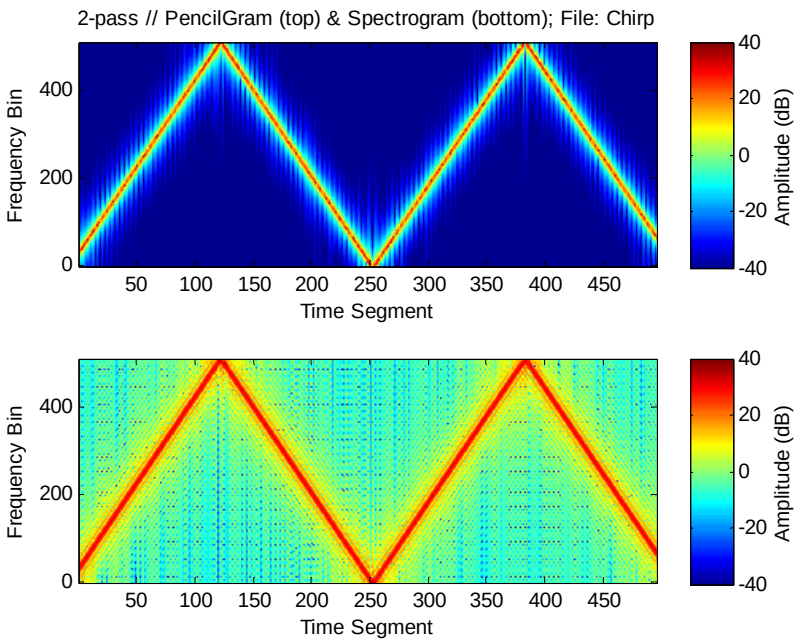

Figure C-1. Pencilgram (upper subplot) and Spectrogram (lower subplot) of a chirp (swept frequency) input test signal; 2x28=56 complex exponential components requested for the pencilgram.

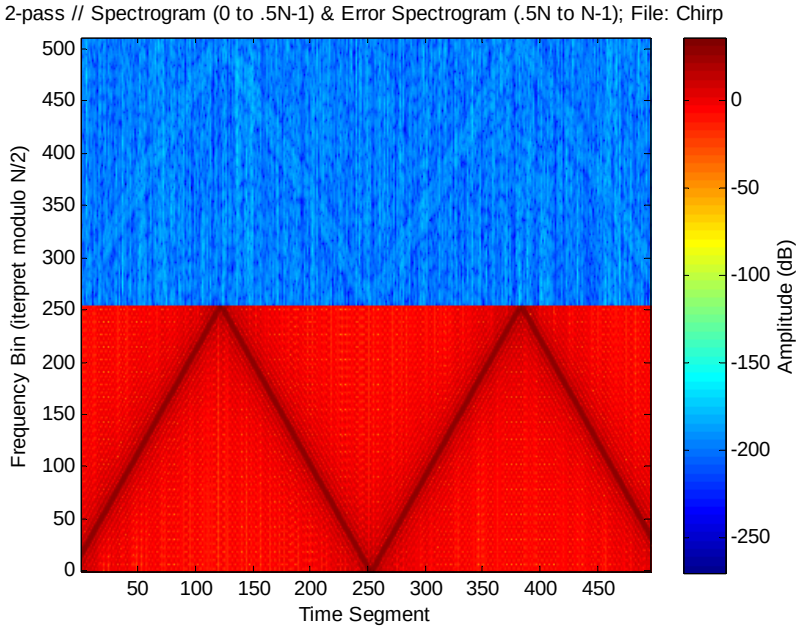

Figure C-2. Spectrogram of error signal (bins .5N to N-1) and spectrogram of chirp (swept frequency) input test signal (bins 0 to .5N-1); 2x28=56 complex exponential components requested for the pencilgram.

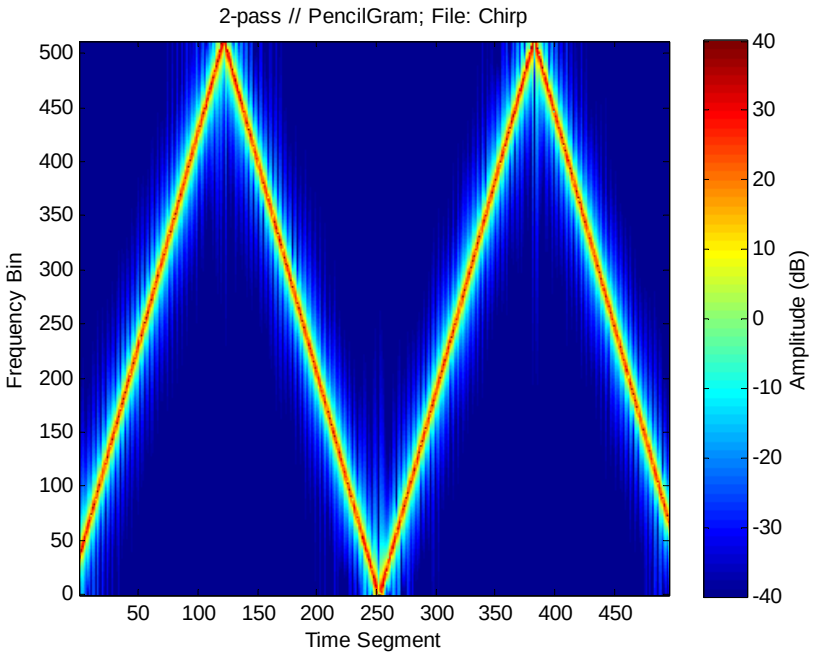

Figure C-3. Pencilgram of a chirp (swept frequency) input test signal; 2x28=56 complex exponential components requested for the pencilgram.

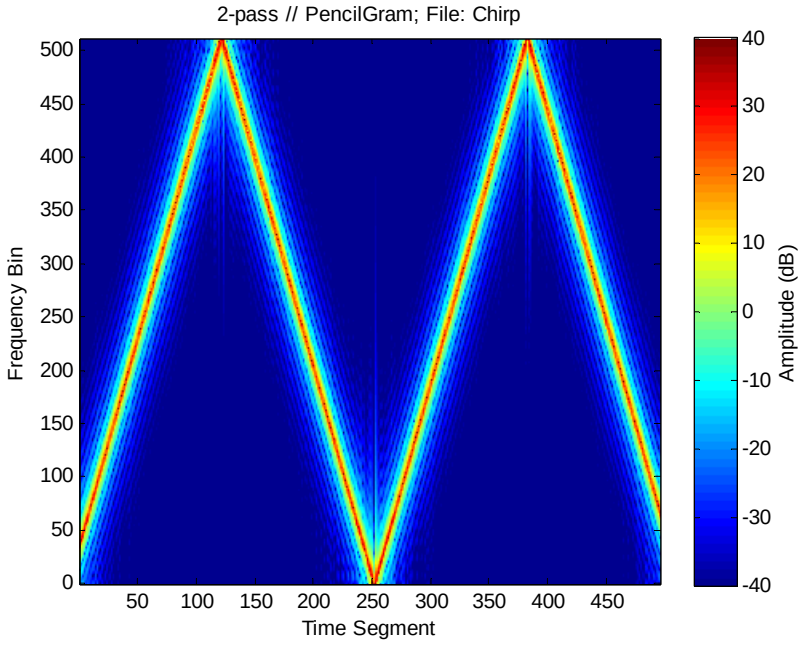

Figure C-4. Pencilgram of a chirp (swept frequency) input test signal; 2x28=56 complex exponential components requested for the pencilgram. Left sided: X = X - exp(-j*W*L)*exp(alphak*(L-1))*exp(j*Wk*(L-1))*r(k)*exp(j*ph(k)).*F (See Appendix).

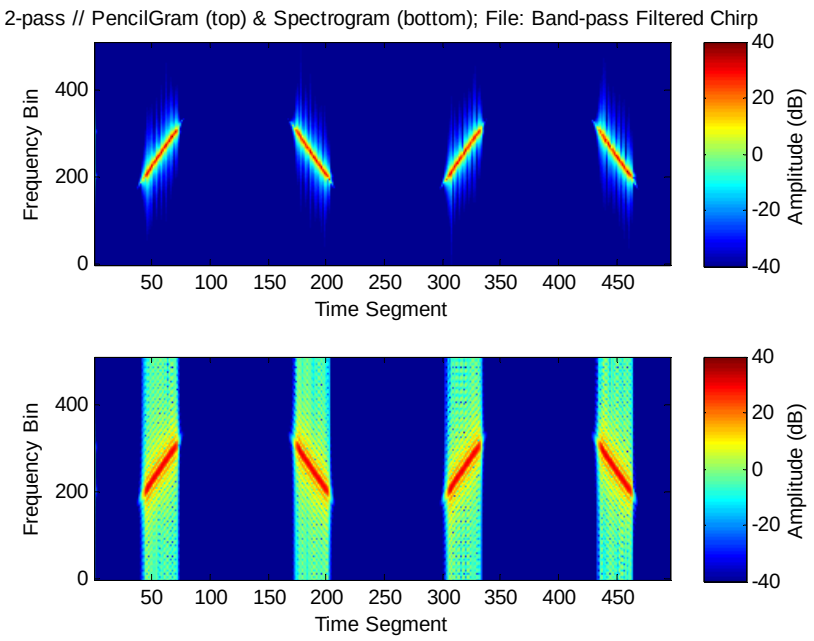

Figure FC-1. Pencilgram (upper subplot) and Spectrogram (lower subplot) of a band-pass filtered chirp (swept frequency) input test signal; 2x28=56 complex exponential components requested for the pencilgram.

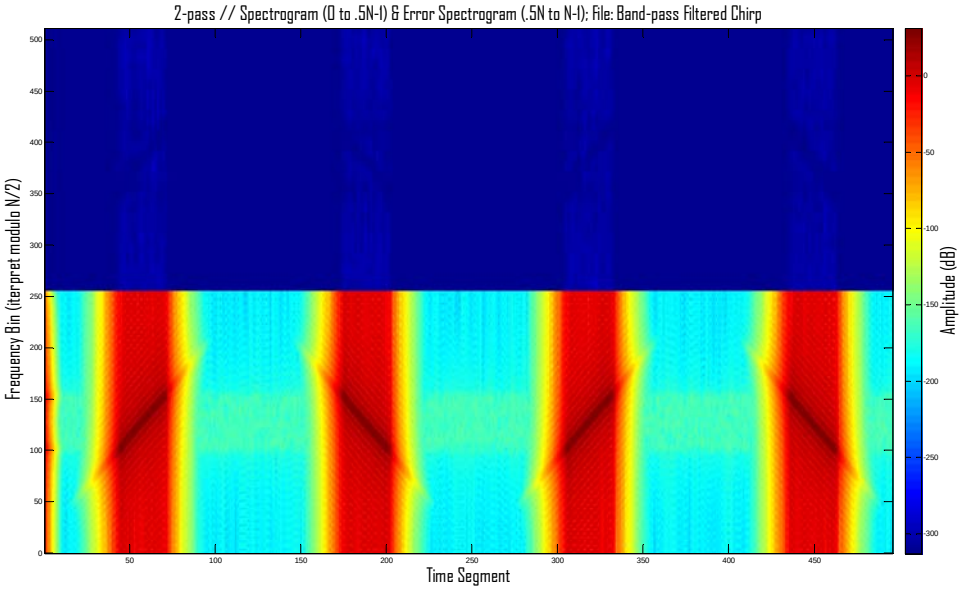

Figure FC-2. Spectrogram of error signal (bins .5N to N-1) and spectrogram of filtered chirp (swept frequency) input test signal (bins 0 to .5N-1); 2x28=56 complex exponential components requested for the pencilgram.

3.2.5 Multi-Segment Speech Signal

The last results presented in this section are obtained for a specific speech signal selected from the TIMIT database, file faks0_sa1.wav. This is a fairly clean speech signal of a short utterance (3 or 4 seconds) from a female speaker, sampled at 8000 samples per second. In general, speech represents a "spectrally diverse" signal containing many components including some that are both narrow- and wide-band nature. As a spectrally rich signal, it also serves to demonstrate the utility of the 2-pass iteration technique previously developed and used in this research to enhance MP model and signal decomposition accuracy.

In Figures SP-1a and SP-1b, we demonstrate signal model and decomposition enhancement obtained via 2-pass iteration. In the first figure, we show the spectrograms of both the original speech (lower portion) and the model error (upper portion) when two iterations of decomposition are performed. It is noted that relative to using one iteration as seen in Figure SP-1b, the model error is significantly reduced by the second iteration.

For comparative analyses, the pencilgram and spectrogram of the selected speech signal are presented in Figure SP-2. The amplitude range for these plots have been set from -70 to +10 dB. Observe that the pencilgram provides significantly enhanced frequency resolution relative to the FFT-based spectrogram. This is particularly helpful in the analyses of speech signals, given the harmonic content present in the signal. Speech waveforms can be described as having voiced, unvoiced and silence regions, along with transitions between these regions, as the signal progresses in time. The voiced regions and corresponding segments tend to have this harmonic structure. These regions are of particular interest to researchers for a variety of applications including automated speaker identification and automated speech recognition.

In general, the amplitude range for any time-frequency representation must be carefully selected, and the more useful ranges are test signal dependent. A new amplitude range of -40 to +40 dB has been selected for the pencilgram presented in Figure SP-3. It can be observed in this and the previous figure, the pencilgram exhibits spectral energy across a large portion of the spectrum for some time segments (e.g., between 370 and 400). Conversely, in the FFT-based spectrogram, these wide-band events do not appear as prominently. The question then arises as to the significance of these events, and whether or not they accurately portray the true underlying spectral content.

One possibility is that the potential inaccuracy is a result of the omitted phase factor, $e^{j\omega L}$, for each left-sided component. Initial comments can be made regarding this possibility by referring to Figure SP-4. In this figure, the pencilgram has been generated with the inclusion of this factor. Referring to the figure, although there are amplitude ripples in the frequency dimension, the wide-band events are still present.

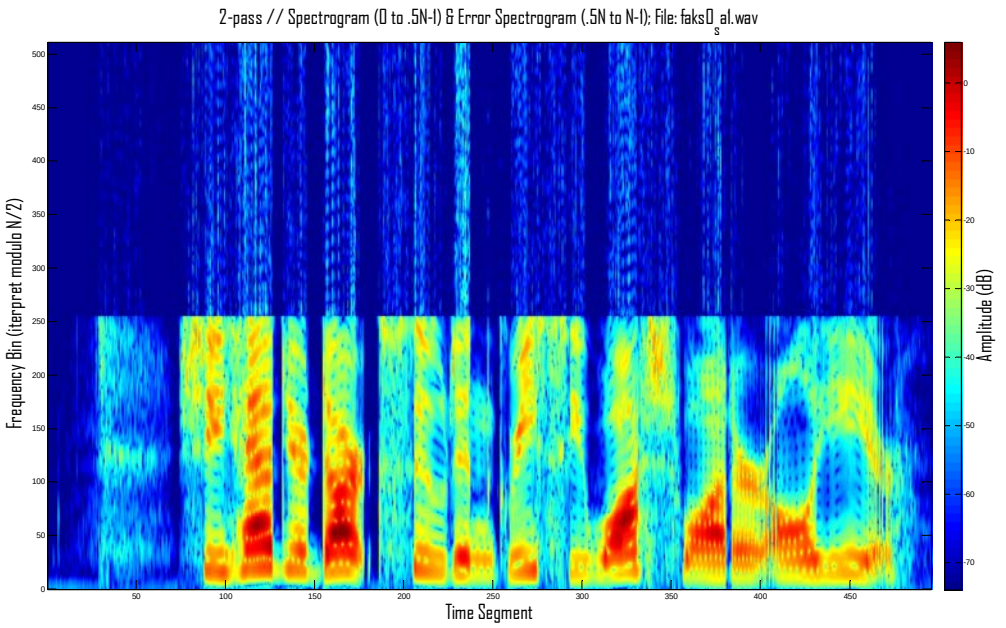

Figure SP-1a. 2-pass Matrix Pencil decomposition; spectrogram of error signal (bins .5N to N-1) and spectrogram of a speech input test signal (bins 0 to .5N-1); $K_c = 28$ complex exponential components requested for the decomposition for each iteration.

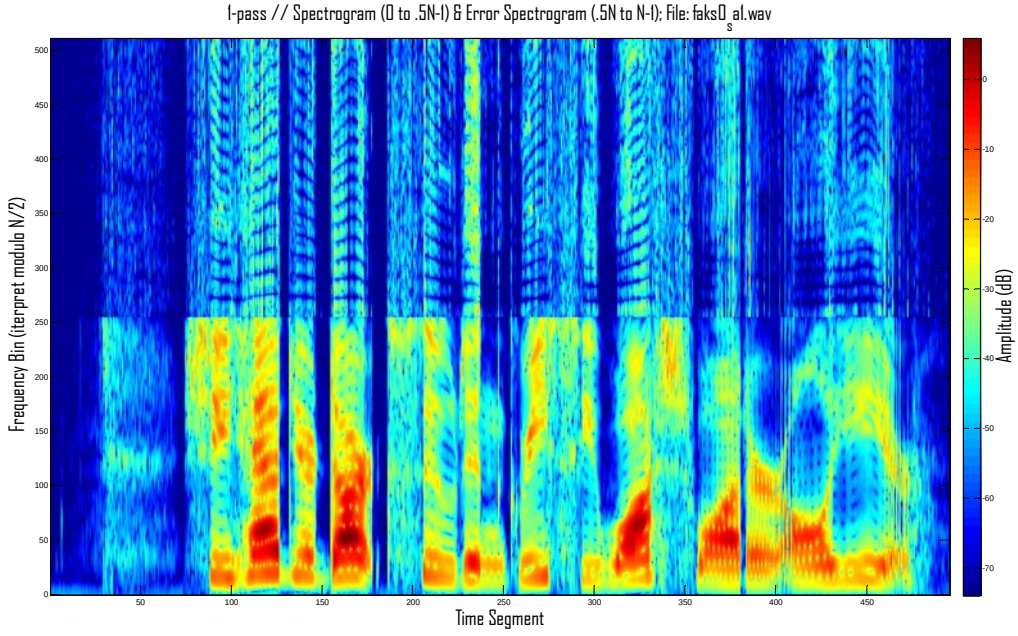

Figure SP-1b. 1-pass Matrix Pencil decomposition; spectrogram of error signal (bins .5N to N-1) and spectrogram of a speech input test signal (bins 0 to .5N-1); $K_c = 28$ complex exponential components requested for the decomposition.

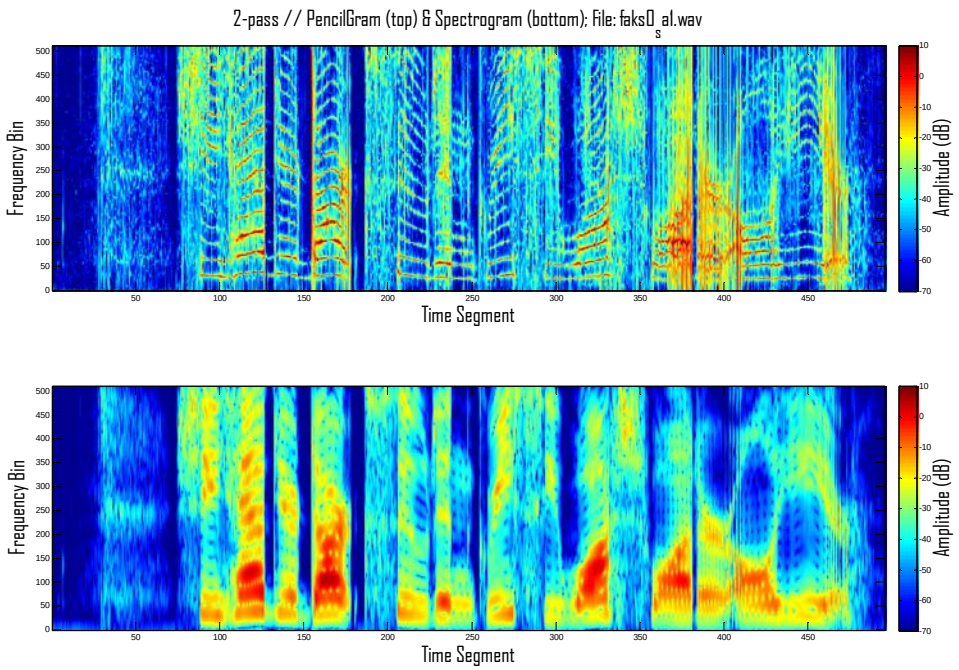

Figure SP-2. Pencilgram (upper subplot) and spectrogram (lower subplot) of a speech input test signal; 2x28=56 complex exponential components requested for the pencilgram.

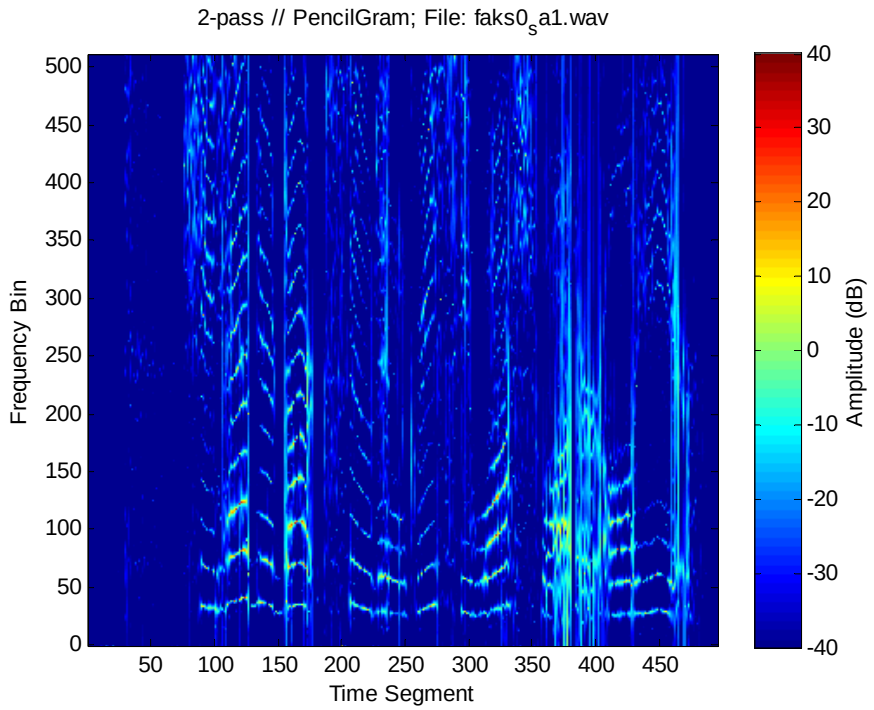

Figure SP-3. Pencilgram of a speech input test signal; 2x28=56 complex exponential components requested for the pencilgram.

Regardless of the accuracy issue, it is interesting to note that these events can be selectively diminished or removed in the pencilgram as a direct characteristic of the MP algorithm. Because each component resulting from the MP algorithm is parameterized as previously described, those components having large values of $|\alpha|$ can be detected and handled differently than other components. For example, only those components with values of $|\alpha|$ less than some specified value can be used to generate the pencilgram. This is the case shown in Figure SP-5. Here, components with values less than .08 in magnitude were used. Note that this has a significant effect in the wide-band event regions previously identified (e.g., segments 370 to 400).

In general, a wide variety of pencilgrams could be conceived and presented. Rather than component selection based on α value, any other parameter or combination of parameters could be used to cue other weightings or handling of the associated components.

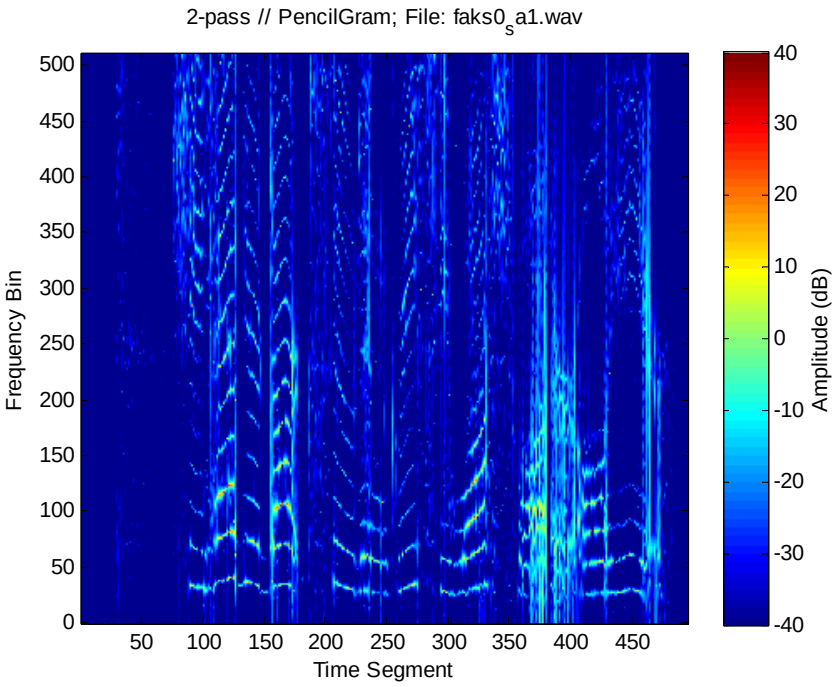

Figure SP-4. Pencilgram of a speech input test signal; 2x28=56 complex exponential components requested for the pencilgram. Left sided: X = X - exp(-j*W*L)*exp(alphak*(L-1))*exp(j*Wk*(L-1))*r(k)*exp(j*ph(k)).*F (see Appendix).

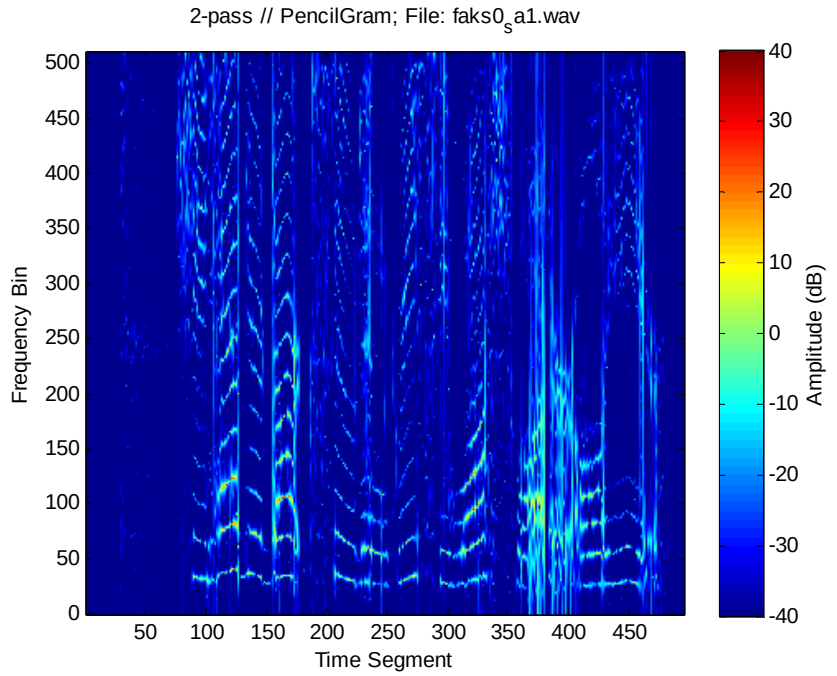

Figure SP-5. Pencilgram of a speech input test signal; 2x28=56 complex exponential components requested for the pencilgram; α magnitudes less than .08 only.

4.0 Summary, Discussions and Future Work

Motivated by the effectiveness of the Matrix Pencil (MP) algorithm in decomposing short-term but otherwise spectrally rich speech segments, a new, high-resolution time-frequency representation has been conceived. Background on the application of the MP algorithm to speech is given in [Haddad]. The MP algorithm is characterized as a method of decomposing an input signal segment into constituent decaying and/or growing complex exponentials in the sequence domain, with corresponding poles in the z-transform domain. Knowledge of the relationship between the z-domain and the Fourier domain lends further credence to the potential for a new Fourier representation. Investigations into the nature of z-domain poles in general, leads to a method of achieving a highly desirable characteristic in the new representation. This characteristic is referred to herein as a reduced bandwidth representation. As introduced in this report, by properly augmenting the signal model using additional poles, component bandwidths are significantly reduced. In the sequence domain, this augmented signal model is describable as a conjugate-symmetric extension of the samples within any given signal segment. This effective window expansion mitigates adverse effects of data windowing by more accurately modeling many practical signals. One important example of where signal model enhancement occurs is for segmented sinusoidal components. The enhanced model not only allows for modeling the components as eternal sinusoids, it also allows for a corresponding representation in the Fourier domain that is essentially a Dirac delta function as predicted by theory. Conversely, existing techniques either model all components of a segment as sinusoidal, or do not yield infinitesimal bandwidths in the Fourier domain for sinusoidal components. Moreover, without reduced bandwidth representation, the remaining complex exponential components would otherwise result in wide-band content in the Fourier domain that interferes with the visualization and potential detection of other signal components.

In addition to presenting the mathematical development of the reduced bandwidth representation, a specific application is also described. The MP algorithm has been used with this new representation to create what we refer to as the pencilgram, named in recognition of the algorithm. As with many time-frequency tools, subjective performance evaluations have been performed. Results have been presented for a variety of stressing waveforms, including tones, swept tones and a representative speech signal. The achieved frequency resolution at unprecedentedly small segment lengths as shown in the examples clearly justifies both use of and further investigations into the properties of the pencilgram.

4.1 Existing Signal Extension Models

Techniques that model the signal outside the extent of the analysis window do already exist in the literature. The most well known but sometimes overlooked is that of the DFT. The DFT is describable as a model-based method, and as a related algorithm, the same is true for the FFT. The DFT models the samples in the signal segment as the weighted summation of an

orthogonal set of sinusoids. However, it also models the overall signal as consisting of repeated consecutive segments that are identical to the segment being analyzed. Thus the analysis window is in effect, expanded to include all other samples. The problem is the accuracy of such an expansion model. It is rarely the case that the segment being analyzed is extracted from a sequence that is periodic with period *L* samples (*L* being the number of samples in the segment).

In [Kay], a spectral estimate is discussed that models exponential decaying components outside the analysis window and is referred to in the publication as the "symmetric envelope exponential model". The corresponding extended signal $\hat{x}(t)$ is presented as a continuous-time signal comprised of *p* components, and the corresponding Fourier transform is given in the reference as

$$\hat{X}(f) = \sum_{m=1}^{p} A_m \exp(j\theta_m) \frac{2\alpha_m}{\alpha_m^2 + (2\pi[f - f_m])^2} \quad , \tag{4-1}$$

with component amplitudes A_m, phases θ_m (in radians), damping factors α_m, and frequencies f_m (in Hz). The parameters of the component exponentials are found via the Prony method as described in the paper. The paper describes Eq. (4-1) as being one possible Prony spectrum and is generated under the assumption that all damping factors are negative so that the components are decaying exponentials.

This is in contrast to our sampled signal representation which accounts for both decaying and growing components as previously described. For comparison, corresponding to each term of Eq. (4-1), the reduced bandwidth representation simplifies from Eqs. (2-1) and (3-5) to

$$S_{a_i}(e^{j\omega}) = 0.5A_i \frac{e^{\alpha_i} - e^{-\alpha_i}}{2\cos(\omega - \omega_i) - (e^{\alpha_i} + e^{-\alpha_i})} \quad , \tag{4-2}$$

for right-sided (decaying with increasing index) components and

$$S_{a_k}(e^{j\omega}) = -0.5A_k \frac{e^{\alpha_i} - e^{-\alpha_i}}{2\cos(\omega - \omega_i) - (e^{\alpha_i} + e^{-\alpha_i})} \quad , \tag{4-3}$$

for left-sided (growing with increasing index) components. These terms would be summed over both *i* and *k* to obtain the overall reduced bandwidth Fourier representation, $S(e^{j\omega})$. Note that the frequency, ω, is in normalized radians, and can be converted to Hz with knowledge of the sampling rate, F_s, used to acquire a corresponding continuous-time signal. Specifically, the conversion is $= 2\pi f / F_s$. (See also [Oppenheim].) It should also be pointed out for clarity that some acquired signals have been translated in frequency either prior to or as a result of the sampling process. This also should be taken into account for correct interpretation of converted frequencies.

4.2 Future Work

A special issue that occurs with the reduced bandwidth representation is the need to properly handle the nascent Dirac delta functions that can arise. Having such delta functions creates the problem of determining how to display segments with such components on the same display as all other segments. Another related problem is how to associate the weights of these delta functions with the displayed amplitudes. Various ways could be conceived to handle nearly sinusoidal components as special cases. A rudimentary way of addressing this issue is to use the FFT of the segment to limit the amplitudes of the reduced bandwidth representation. An example of this is presented in Figure F-1. In this example, the segment is weighted with a Hanning window, and then zero-padded to *N* samples in length. For comparison, see also Figure KM-2. Note that most of the pencilgram remains unchanged, with the exception of the tone components located at 0.2π, 0.4π and 0.42π radians. In addition to loss in resolution, a disadvantage of this approach is the potential for undesired reductions in amplitude for otherwise low level regions as seen in the figures.

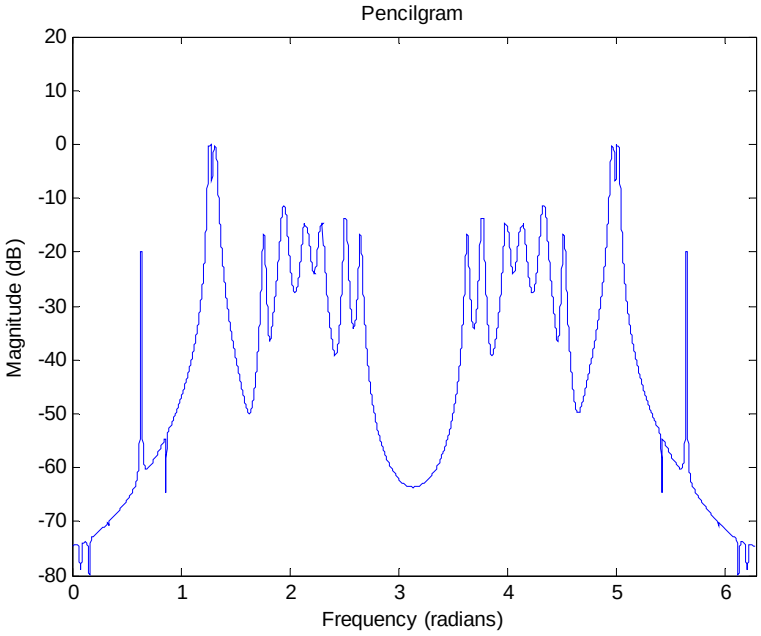

Figure F-1. An example modified pencilgram of the test signal identified in [Kay]; Kc = 18 complex exponential components requested with 5000 samples on the unit circle.

The subjective results presented in this research serve as motivation to further pursue such algorithm refinements and to define objective performance metrics for applications of interest. Objective performance measures will generally be application specific. For example, for potential application in co-channel interference mitigation, a specific goal may be to detect and remove undesirable tones from the underlying signal of interest. Such tones can have adverse effects in demodulation and other subsequent signal processing steps. In this example, signal-to-interference (S/I) ratios along with detection and false alarm rates can serve as metrics to determine if representations such as the pencilgram can be used to enhance detection performance. Based on interests in methods of reassignment as in [Gardner], the pencilgram may be useful as the first step in such techniques, rather than starting with e.g., the FFT. Other potential application examples include Fourier domain filtering, signal pre-conditioning, automated speech and speaker identification and various pattern recognition problems. Likewise, appropriate metrics can be defined to measure possible performance enhancements for these applications. It should also be noted that by identifying appropriate metrics, the merit of using other methods of signal decomposition could be investigated. In particular, it is pointed out that models that allow for higher order signal components could be investigated. Techniques to utilize such models may be possible based on known continuity properties across consecutive segments. These properties may serve as constraints, and along with applicable optimization methods, may lead to other reduced bandwidth representations or to a useful minimum bandwidth representation.

References

The following references are given as representative sources. The list is by no means complete given the numerous publications in this subject area. The volume of literature is a reflection of the large number of application areas for frequency analyses and related methods.

[Boashash] B. Boashash, B. Lovell, and P. Kootsookos, "Time-Frequency Signal Analysis & Instantaneous Frequency Estimation – Methodology, Relationships and Implementations," ISCAS, 1989.

[Brown] S. C. M. Brown, J. C. Bennett, "Reduced Bandwidth Algorithm for Near Field Imaging of Tree Targets Using Synthetic Aperature Radar," *IEE Proc. Radar, Radar, Sonar, Navig.,* Vol. 148, No. 5, October, 2001.

[Cohen] Leon Cohen, *Time Frequency Analysis*, Prentice Hall, 1995.

[Gardner] Timothy J. Gardner, Marcelo O. Magnasco, "Sparce Time-Frequency Representations," *Proceedings of the National Academies of Science of the United States of America*, Vol. 103, No. 16, April 18, 2006.

[Haddad] Darren Haddad, "The Matrix Pencil and its Application to Speech Processing," AFRL-IF-RS-TR-2007-89, March, 2007.

[Kay] Steven M. Kay, Stanley Lawrence Marple Jr., "Spectrum Analysis – A Modern Perspective," *Proceedings of the IEEE*, Vol. 69, No. 11, November, 1981, pp. 1380-1419.

[Noga] Andrew J. Noga, "Numerical Demodulation Enhancements," RL-TR-96-91, June, 1996.

[Oppenheim] Alan V. Oppenheim, Ronald W. Shafer, John R. Buck, *Discrete-Time Signal Processing*, 2nd Edition, Prentice Hall, 1999.

[Sarkar] Tapan K. Sarkar, Odilon Pereira, "Using the Matrix Pencil Method to Estimate the Parameters of a Sum of Complex Exponentials," IEEE Antennas and Propagation Magazine, Vol. 37, No.1, February, 1995, pp. 48-55.

[Suter] Bruce W. Suter, *Multirate and Wavelet Signal Processing*, Academic Press, 1998.

List of Acronymns

DFT	Discrete Fourier Transform
FFT	Fast Fourier Transform
FIR	Finite Impulse Response
FM	Frequency Modulation
FSK	Frequency Shift Keyed
Hz	Hertz (cycles per second)
IIR	Infinite Impulse Response
MP	Matrix Pencil
ROC	Region of Convergence
S/I	Signal-to-Interference Ratio

Appendix: Sample Pencilgram Code

The following Matlab (The Mathworks, Inc.) code is provided for informational purposes only; there are no direct or implied warrantees regarding any aspects of the code. For examples presented in this report, the pencil parameter was set as $p = L/2$.

```
function [X, xr] = mp_gram_complex(x,Kc,p,L,N)

%
% usage: [X, xr] = mp_gram_complex(x,Kc,p,L,N)
%
% parameters: x  - data samples; L <= length(x)
%             Kc - estimated/specified number of exponentials
%             p  - pencil parameter (choose p >= Kc, p <= L-Kc)
%             L  - length of signal analyzed (samples, L < 2000 or so)
%             N  - number of discrete frequencies around the unit circle
%
%
% returned: X  - unit circle response (complex valued)
%           xr - reconstructed estimate of x
%
% AJNoga, December, 2008; this version handles complex-valued inputs.
%

% unnecessary dimensionality change (for consistency with the original math)
if(size(x,2) ~= 1)
    x = x';
end

% parameter for ensuring singular pairs are retained in tact
PCT = .01;

% check input
if p < Kc
   error('mp_gram_complex - Choose p >= Kc');
end
if L-Kc < p
   error('mp_gram_complex - Choose L-Kc < p');
end

% form the matrix X0; alternatively, can use the following line
% X0 = hankel(x(1:p),x(p:L));
X0 = zeros(L-p,p+1);
for i=1:L-p;
   X0(i,1:p+1) = x(i:p+i-1+1);
end

% singular value decomposition of X0
[U,Sd,V] = svd(X0);
dS      = diag(Sd);
```

```
% take care of double poles
if(Kc+1 <= p)
   if(dS(Kc) ~= 0)
      if((dS(Kc)-dS(Kc+1))/dS(Kc) < PCT)
         Kc = Kc + 1
      end
   end
end

% truncate to Kc singular values
U0        = U(1:p-1,1:Kc);
U1        = U(2:p,1:Kc);

% equivalent to calculating the eigenvalues of X02Kinv*X1
% (row selections of decomposition rather than column selections of data)
lambda    = eig(pinv(U0)*U1);

% "equation" matrix, A, for least-squares estimation of amplitudes, phases
for ii=1:L
   for jj=1:Kc
      A(ii,jj)=lambda(jj)^(ii-1);
   end
end

% least-squares solution matrix
T = inv(A'*A)*(A'); % same as inv(conj(A')*A)*conj(A');

% project data onto "basis functions" to get the solution, x
x = T*x;

% least squares estimates of phases and amplitudes
r   = abs(x);
ph  = angle(x);

% generate X and signal estimate, xr
X  = zeros(N,1);
W  = ((0:N-1)*2*pi/N)';
n  = (0:L-1)';
xr = zeros(L,1);
z  = exp(j*W);
for k = 1:Kc
   a      = lambda(k);
   alphak = log(abs(a));
   Wk     = angle(a);

   % evaluate on the unit circle
   F  = real(z./(z-a) - .5);
   if(alphak < 0) % decaying component
      X  = X + r(k)*exp(j*ph(k)).*F;
   else % growing component
      X  = X - exp(alphak*(L-1))*exp(j*Wk*(L-1))*r(k)*exp(j*ph(k)).*F;
   end
   xr = xr + x(k)*(lambda(k).^n); % regenerate signal
end
```